Article

Not peer-reviewed version

Comparative Study on Hot Metal Flow Behaviour of Virgin and Rejuvenated Heat Treatment Creep Exhausted P91 Steel

Shem Maube * , Japheth Obiko * , Josias Van der Merwe , Desmond Klenam , Fredrick M Mwema , Michael Bodunrin

Posted Date: 28 February 2023

doi: 10.20944/preprints202302.0502.v1

Keywords: P91 steel; Rejuvenation Heat treatment; Creep Exhausted; Constitutive equation; hot deformation

Preprints (www.preprints.org) | NOT PEER-REVIEWED | Posted: 28 February 2023 doi:10.20944/preprints202302.0502.v1

Article

Comparative Study on Hot Metal Flow Behaviour of Virgin and Rejuvenated Heat Treatment Creep Exhausted P91 Steel

Shem Maube [1,*], Japheth Obiko [2,*], Josias Van der Merwe [3,4], Fredrick Mwema [1], Desmond Klenam [3] and Michael Bodunrin [3,4]

[1] Department of Mechanical Engineering, Dedan Kimathi University of Technology, Nyeri, Kenya
[2] Department of Mining, Materials and Petroleum Engineering, Jomo Kenyatta University of Agriculture and Technology, Nairobi, Kenya
[3] School of Chemical and Metallurgical Engineering, Faculty of Engineering and the Built Environment, University of the Witwatersrand, Johannesburg, South Africa.
[4] DSI-NRF Centre of Excellence in Strong Materials, University of the Witwatersrand, Johannesburg, South Africa
* Correspondence: smaube@gmail.com (S.M.); japheth.obiko97@gmail.com (J.O.)

Abstract: This article reports on the comparative study of the hot deformation behaviour of virgin (steel A) and rejuvenated heat treatment creep-exhausted (steel B) P91 steels. Hot uniaxial compression tests were conducted on the two steels at the deformation temperature range of 900°C-1050°C and a strain rate range of 0.01-10s^{-1} to 0.6 strain using Gleeble® 3500 equipment. The results showed that the flow stress largely depends on the deformation conditions. The flow stress for the two steels increased with an increase in strain rate at a given deformation temperature and vice versa. The flow stress-strain curves exhibited a dynamic recovery as the softening mechanism. The material constants determined using Arrhenius constitutive equations were: stress exponent was: steel A (5.76) and steel B (6.67), and the apparent activation energy was: steel A (473.1 kJ mol-1) and steel B (564.5 kJmol-1). From these results, steel A exhibited better workability than steel B. Statistical parameters analyses showed that the flow stress for the two steels had a good correlation between the experimental and predicted data. Pearson's correlation coefficient (R) was: steel A (0.97) and steel B (0.98). The Average Absolute Relative Error (AARE) values were: 7.62% (steel A) and 6.54% (steel B). The study shows that the Arrhenius equations can effectively describe the flow stress behaviour of P91 steel, and this method is applicable for industrial metalworking process.

Keywords P91 steel; rejuvenation heat treatment; creep exhausted; constitutive equation; hot deformation

1. Introduction

P91 steel belongs to a family of 9–12% Cr ferritic creep resisting steels [1]. The steel was initially developed in the 1970s for application in steam generators of fast breeder reactors by Oak Ridge National Laboratory [2], [3]. At present P91 steel has wide application in high-temperature and high pressure components such as headers, heat exchangers, water-wall tubing and piping systems of fossil-fuel power plants[4], [5]. The suitability of this steel for these applications is due to its superior thermal mechanical properties. These include high corrosion resistance, good weldability and low thermal expansion [6]. The steel also has toughness and good creep performance at temperatures up to 600 °C and 100,000 hours. This is due to carbides that evolve during tempering heat treatment during production [7], [8].

After prolonged service, the steel experiences internal damage due to microstructural changes from long-term exposure to high temperatures under stress. These microstructure changes cause a detrimental effect on mechanical properties, especially toughness and degradation of creep properties [9][8]. At the end of the design lifetime, the creep-exhausted components are replaced. The high cost of replacing these components has attracted research interest in extending the service life of creep-exhausted components.

Restoration of the microstructure of degraded components has been achieved through various thermal procedures such as heat treatment and hot isostatic pressing [10]. Thermal rejuvenation procedures can modify the material's microstructure, thus improving mechanical properties[11]. Heat treatment schedules may cause grain refinement and re-establishment of the original microstructure. The heat treatment can therefore restore the material properties of service-exhausted components [12]. However, there is scanty information about the effect of rejuvenation heat treatment on metal flow behaviour, especially P91 steel.

In 9–12% Cr ferrite steels, heat treatment is generally by normalising, cooling and tempering processes [13]. Normalising is conducted above the upper critical temperature, Ac_3, and tempering below the lower critical temperature, Ac_1 [14]. Various authors [2], [8], [14]–[17] have applied different normalisation and tempering temperatures for P91 steel within the Ac_3 and Ac_1 requirements. Pandey *et. al.* [2] reported phase transformation temperatures of P91 as 810°C to 825°C (Ac_1) and 912°C to 930°C (Ac_3). According to Abe [18], the Ac_1 was (800 to 830°C) and Ac_3 (890 to 940°C) in P91. The variations in heat treatment temperatures of P91 are due to minor differences in chemical composition (especially Ni + Mn), rate of heating and prior austenite grain boundaries(PAGBs) [17]. American Society of Mechanical Engineers (ASME) [18] recommended austenitisation temperature of 1040 to 1080°C and tempering at 730 to 780°C in P91 pipes.

In 9-12%Cr ferritic steels, creep deformation mechanisms are mainly associated with changes in the microstructure. These microstructure changes cause a reduction in dislocation density, migration of sub-grain boundaries, formation of new secondary phases (Laves and Z-phase) and growth of sub-grain structure [19]. During creep, the sub-grains grow, causing a decrease in the creep strength in 9-12%Cr steels while Laves phase coarsens around $M_{23}C_6$ carbides along the PAGBs reducing their pinning effect [20]. Hence, reducing the strengthening mechanism.

Heat treatment of P91 steel produces a tempered lath martensite structure with carbides such as $M_{23}C_6$ (M = Chromium, Iron, Tungsten and Molybdenum) and MX (M =Niobium, Vanadium and X-carbon) [2]. During normalisation, the homogenisation of the microstructure occurs, causing an untampered lath microstructure with a small number of precipitates and a high dislocation density. Tempering causes the precipitation of the $M_{23}C_6$ carbides along the grain boundaries and MX particles in the matrix [20]. The high dislocation density and $M_{23}C_6$ precipitates are responsible for the pinning of lath boundaries, while MX precipitates prevent dislocation movement [2], [21]. The heat treatment process, therefore, restores the effects of the creep deformation process and provides a stable microstructure that enables P91 steel to achieve high creep strength [6].

Rejuvenation heat treatment, as mentioned earlier, can be used for complete recovery of material properties and reuse of exhaust components or partial recovery for alternative applications [10]. Should the alternative application require the manufacturing of a new structural part from either processing or machining, it is imperative to understand the response of the effect of rejuvenation heat treatment on creep-exhausted steel to thermomechanical processing parameters. Hence, the study provides the basis for understanding the metal flow pattern during deformation. A comparative study using constitutive models developed from the hot deformation behaviour of steel A and steel B can be used for this analysis [22].

For example, phenomenological constitutive models such as Arrhenius equations are widely used to study the metal flow behaviour of various metals and alloys [23]. Examples of such materials include low-carbon steel [24][25], P92 steel [26], nickel-based super alloys [27], alloys of aluminium [24], and magnesium [28]. The accuracy and reliability of a constitutive model in predicting the flow stress form the basis of studying the material process behaviour [29]. These models act as inputs to Finite Element Method codes. These computer codes assist in the simulation and the optimisation of thermomechanical process parameters. The simulation results depend on the accuracy and dependability of the constitutive models [22], [29].

The objective of the present study was to investigate the flow stress behaviour of steel A and steel B using constitutive equations. The steel B was heat treated by normalisation followed by air cooling, then tempering processes. Isothermal hot deformation tests were then conducted at various strain rates and temperatures to study the flow stress behaviour for the two steels. Experimental flow

Preprints (www.preprints.org) | NOT PEER-REVIEWED | Posted: 28 February 2023 doi:10.20944/preprints202302.0502.v1

stress values were used to develop constitutive equations based on the Arrhenius-type equation. These equations were validated using statistical parameters.

2. Materials and Methods

The P91 steels studied had chemical composition (wt%) of Cr-9.189 C-0.1 Mn-0.447 Mo–0.885 V–0.191 Nb-0.076 Ni–0.158 Si-0.254 P-0.02 Cu-0.086. Isothermal compression samples were machined from the two steels to a cylindrical shape of diameter 8mm and height 12 mm. The steel B samples were heat treated by austenitising at 1050°C for 40 minutes, air cooling and tempering at 760°C for 2 hrs, as shown in **Error! Reference source not found.**. These are typical heat treatment conditions used during the production process of boiler pipes [16]. Figure 3 (a) and (b) show the optical micrographs of undeformed steel A and steel B. The steel A showed a typical tempered martensitic microstructure with prior austenite grain boundaries (PAGBs) and dispersion of fine precipitates in the matrix. The microstructure of steel B exhibited clear grain boundaries compared to steel A.

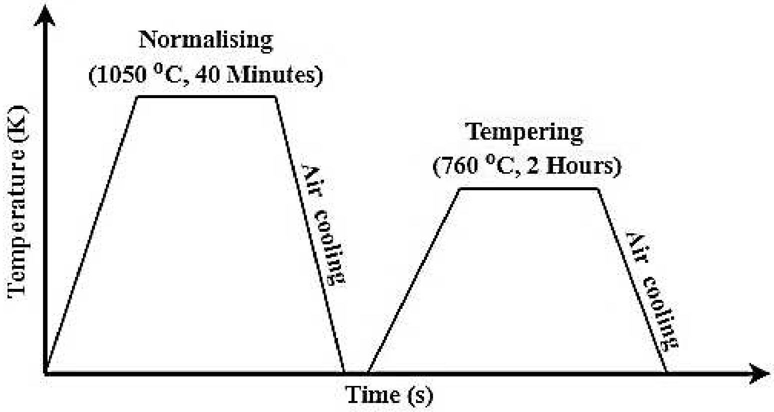

Figure 1. The heat treatment process of creep exhausted P91 steel.

The uniaxial hot compression parameters using Gleeble® 3500 equipment were as follows: deformation temperatures of 900°C, 950°C, 1000°C, and 1050°C and strain rates of $0.01s^{-1}$, $0.1s^{-1}$, $1s^{-1}$, and $10s^{-1}$ to a strain of 0.6. Before testing, an R-type thermocouple was welded at the midpoint on the samples to monitor temperature during the deformation process. **Error! Reference source not found.** is a schematic diagram illustrating the thermal deformation process used in this study. All the specimens were heated at 5°C/s to 1100°C and held isothermally for 180s before cooling to the deformation temperature.

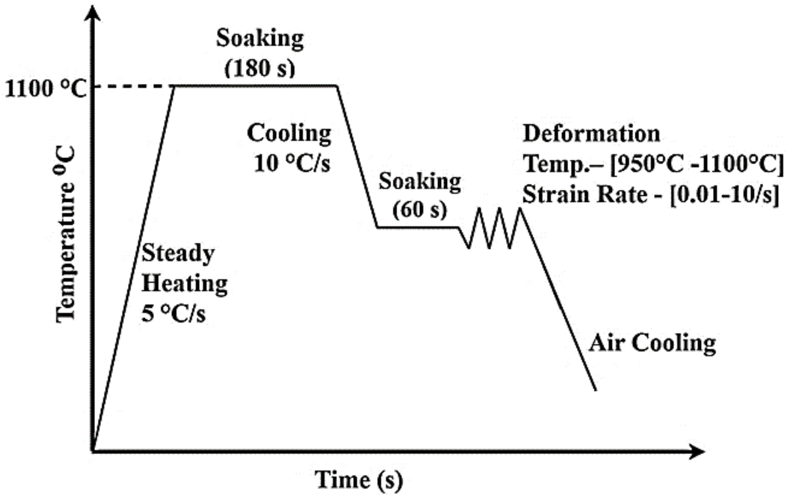

Figure 2. Thermal deformation profile.

doi:10.20944/preprints202302.0502.v1

The deformed samples were cut along the compression axis for microstructural analysis. The specimen was prepared following the metallographic procedures. Etching was done using Villella's reagent solution (1g Picric acid + 5 ml HCl + 100 ml ethanol).

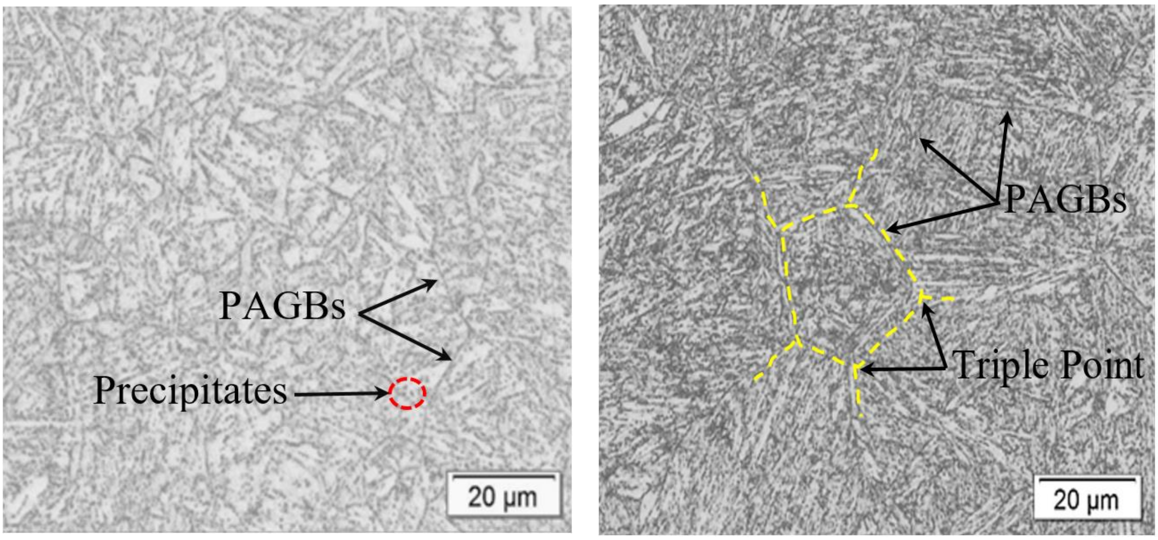

a) b)

Figure 3. The optical micrographs for a) steel A b) steel B.

3. Results

3.1. Flow Stress-Strain Curves

Flow stress-strain curves provide information on metal deformation behaviour during forging. Flow stress-strain curves obtained from the uniaxial compression test are affected by the interfacial friction between the tool and the workpiece. Studies have shown that the interfacial friction at the sample/die interface modifies the force required during deformation [30]. At high strain, the friction effect was more significant, causing inhomogeneous deformation. Hence, barrelling of the sample occurs. Therefore, the flow stress-strain curves should be friction corrected before further analysis. [30], [31].

After the hot compression test, the barrelling coefficient was calculated using the sample geometry size. According to Roebuck *et al.* [32], Equation(1) provides an efficient way of determining the barrelling coefficient, *b*. The allowable values for barrelling should be within the range of $1 < b \leq 1.1$ [33]. These barrelling range values are negligible [34]. **Error! Reference source not found.** shows plots of uncorrected and friction-corrected flow stress curves for the two P91 steels at a temperature of 950°C and strain rate of 0.01 s^{-1}, 0.1 s^{-1}, 1s^{-1}, and 10s^{-1}. The results show that the measured flow stress values were the highest. This flow stress-strain curve variation can be due to the interfacial friction effect experienced at the test sample and anvil interface.

$$b = \frac{h_f d_f^2}{h_o d_o^2} \quad (1)$$

Where, h_o and h_f are initial and final height of the sample and d_o and d_f are the initial and final diameter of the sample.

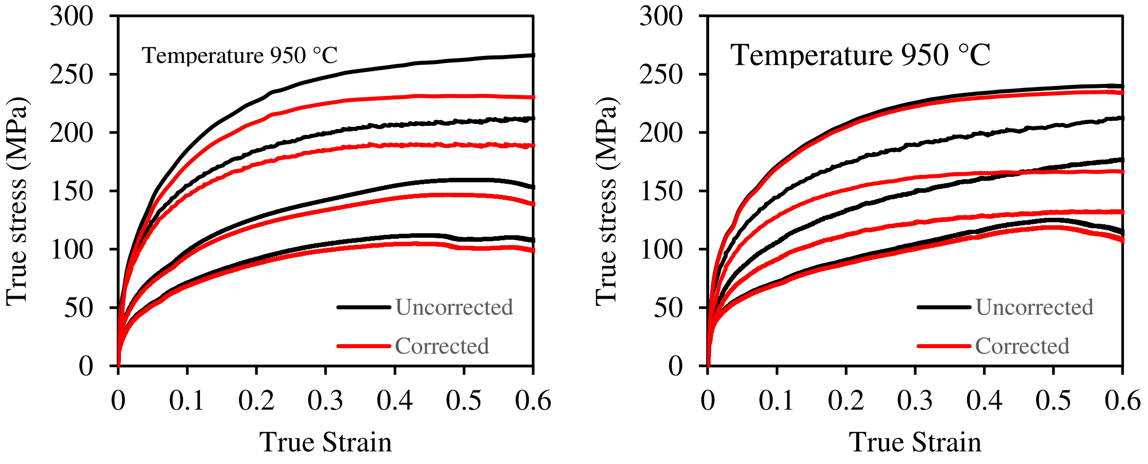

a) Steel A

b) Steel B

Figure 4. Plots of Uncorrected and Corrected flow stress against True strain.

Error! Reference source not found. (steel A) and **Error! Reference source not found.** (steel B) shows friction-corrected flow stress-strain curve at various deformation conditions. The flow stress-strain curves show that the flow stress depends on the strain rate and deformation temperature. For a given strain rate, flow stresses decrease with an increase in the deformation temperature of the two steels investigated. These metal flow patterns may be due to the increase in mobility of grain boundaries as deformation temperature increases [35]. At a given temperature, flow stress increase with an increase in the strain rate. The flow stress-strain curves (**Error! Reference source not found.-Error! Reference source not found.**) show that at the beginning of the deformation process, the flow stress increased rapidly up to a strain of ~0.2. This characteristic flow behaviour occurs due to the rapid generation of dislocation density resulting in a work-hardening deformation mechanism. [36]. At higher strain (>0.2), most flow stress-strain curves for the two steels reached a steady-state condition. This characteristic behaviour of flow curves indicates a balance between work hardening and softening mechanisms, especially dynamic recovery (DRV for these steels [37]. The flow stress-strain curves for the two steels studied did not exhibit a clear peak and subsequent steady-state flow stress caused by DRX [33], [38]. Therefore, for most deformation conditions, the flow curves had increasing flow stress until the start of the saturation stress (σ_{sat}) region. The results show that DRV was the softening mechanism. Similar flow stress-strain curves behaviour results are available in the literature for creep resistant steels [39], [40].

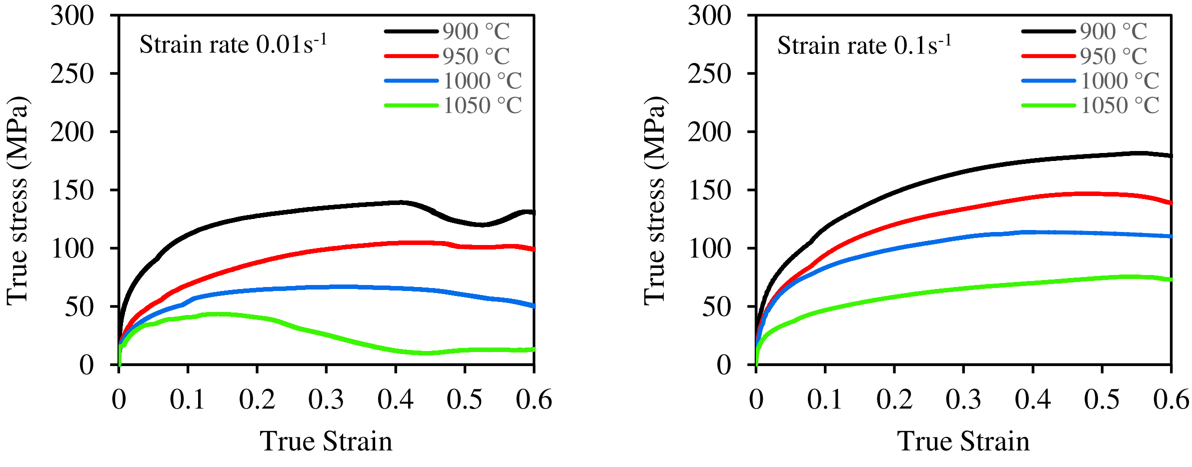

a)

b)

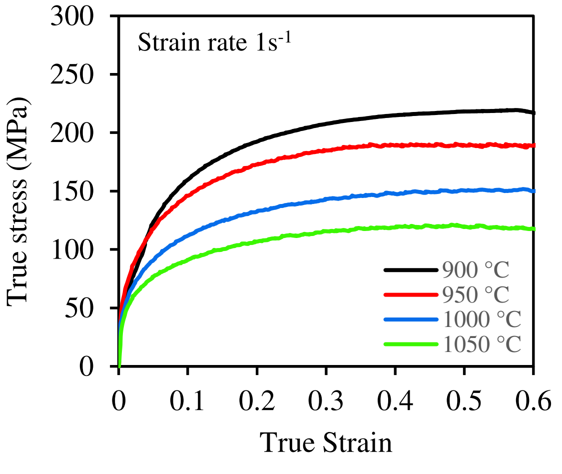

c) d)

Figure 5. Flow stress-strain curve of steel A.

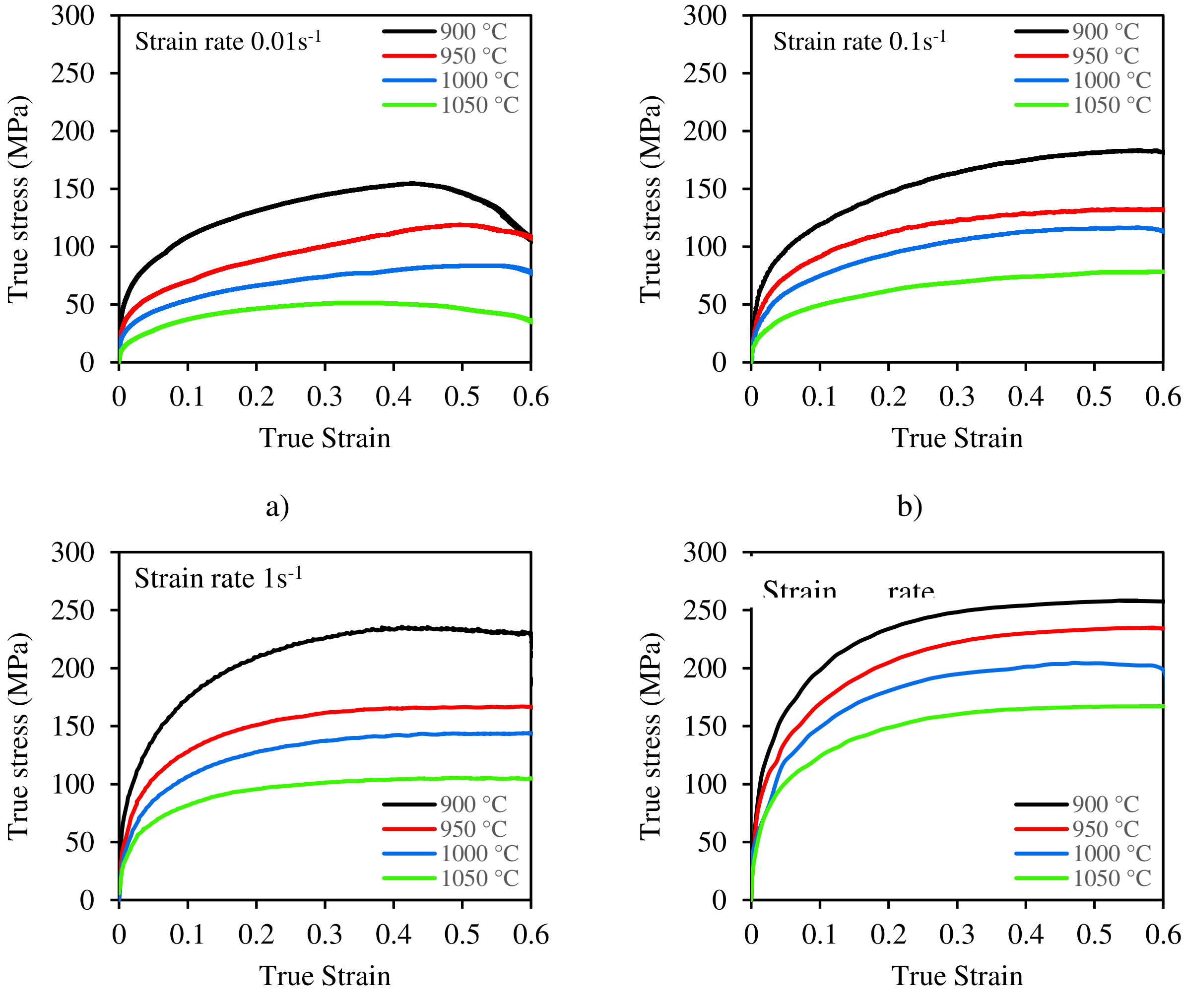

a) b)

c) d)

Figure 6. Flow stress-strain curves of steel B.

3.2. Constitutive Model and Material Constants

Constitutive models accurately predict the flow stress behaviour of metals and alloys during deformation [41]. For example, the Arrhenius equation is widely used to show the relationship between stress, temperature and strain rates during forming [23]. The effect of temperature and strain rate can also be expressed using the temperature-compensated strain rate, the Zener-Hollomon parameter (*Z*) [42].

$$\dot{\varepsilon} = Af(\sigma)exp\left(\frac{-Q}{RT}\right) \tag{2}$$

$$Z = \dot{\varepsilon}\, exp\left(\frac{Q}{RT}\right) \tag{3}$$

Where, σ is flow stress, $\dot{\varepsilon}$ is strain rate, T is absolute temperature (K) and Q is activation energy for hot deformation (kJ/mol), A is a material constant and R is the universal gas constant (8.314 Jmol^{-1} K^{-1}).

$$Z = \dot{\varepsilon}\, exp\left(\frac{Q}{RT}\right) = f(\sigma) = A\sigma^{n'} \tag{4}$$

$$Z = \dot{\varepsilon}\, exp\left(\frac{Q}{RT}\right) = f(\sigma) = A\, exp(\beta\sigma) \tag{5}$$

$$Z = \dot{\varepsilon}\, exp\left(\frac{Q}{RT}\right) = f(\sigma) = A\,[Sinh\,(\alpha\sigma)]^{n} \tag{6}$$

The relationship between the Zener-Hollomon parameter and flow stress, is expressed by Equations (4) to (6). The terms in these equations: n' β, n, and α, are material constants. Equation (4) is the power law applied for low stresses ($\alpha\sigma < 0.8$) as it breaks down at higher flow stress. Equation (5) is the exponential law used for higher stress ($\alpha\sigma > 1.2$) and breaks down at strain rate under 1s^{-1} and high temperature. Equation (6) is a hyperbolic sine function equation developed by Sellars and Tegart [43] to be applicable to a wide range of stresses (both high and low). Equations (4)-(6) can also give Equations (7) and (9):

$$\dot{\varepsilon} = A\sigma^{n'}\, exp\left(\frac{-Q}{RT}\right) \tag{7}$$

$$\dot{\varepsilon} = A\, exp(\beta\sigma)\left(\frac{-Q}{RT}\right) \tag{8}$$

$$\dot{\varepsilon} = A\,[sinh(\alpha\sigma)]^{n}\, exp\left(\frac{-Q}{RT}\right) \tag{9}$$

The constants n' and β are determined by taking logarithms on both sides of Equations (7) and (8). These are presented as Equations (10) and (11). The plots of ln $\dot{\varepsilon}$ versus ln σ (Equation 10) and ln $\dot{\varepsilon}$ versus σ (Equation 11) are used to calculate the material constants n' and β respectively. **Error! Reference source not found.** ((a) and (b)) is a representation of the plots based on flow stress data to a true strain of 0.6.

$$\ln\dot{\varepsilon} = \ln A + n'\ln\sigma - \frac{Q}{RT} \tag{10}$$

$$\ln\dot{\varepsilon} = \ln A + \beta\sigma - \frac{Q}{RT} \tag{11}$$

The stress multiplier α is an adjustable constant. This α-value is obtained from: $\alpha = \beta/n$. The stress exponent, n, and activation energy, Q, are determined by taking logarithms on both sides of Equation (9), which gives Equations (12) and (13). These equations are plotted as ln $\dot{\varepsilon}$ versus ln (sinh ($\sigma\alpha$)) and ln (sinh ($\sigma\alpha$)) versus (1000)/T, as shown in **Error! Reference source not found.** (a and b). The average value of the slopes obtained in these plots gives n and S values for calculating the activation energy Q.

$$\frac{1}{n} = \left[\frac{\partial \ln[sinh(\sigma\sigma)]}{\partial(ln\dot{\varepsilon})}\right]_T \qquad (12)$$

$$Q = RnS = Rn\left[\frac{\partial \ln[sinh(\sigma\sigma)]}{\partial({}^{1}/{}_{T})}\right]_\varepsilon \qquad (13)$$

The relationship between the flow stress and the Zener-Holloman parameter is, as given in Equation (6). The structure factor (A) is determined by taking logarithms on both sides of Equation (6), as in Equation (14). The *A* value is the intercept of the best fit line obtained by plotting ln (Z) versus ln (sinh(ασ)), as shown in **Error! Reference source not found.**.

$$\ln Z = \ln A + n\ln Sinh\ (\alpha\sigma) \qquad (14)$$

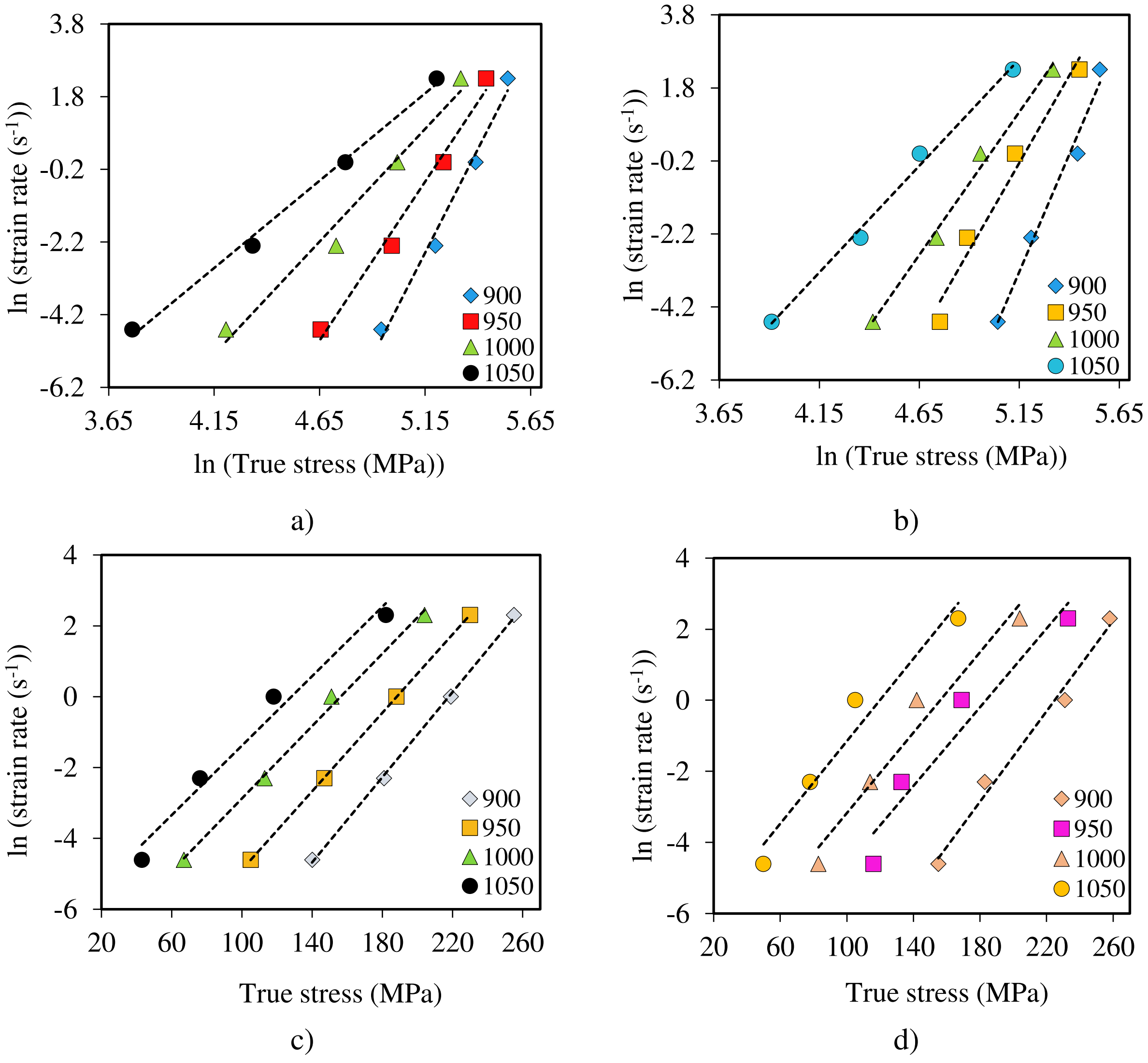

a) b)

c) d)

Figure 7. (a and b) Plots of ln ($\dot{\varepsilon}$) versus ln σ and ln ($\dot{\varepsilon}$) versus σ for determination of n' steel A and steel B and (c and d) for determine of β in steel A and steel B.

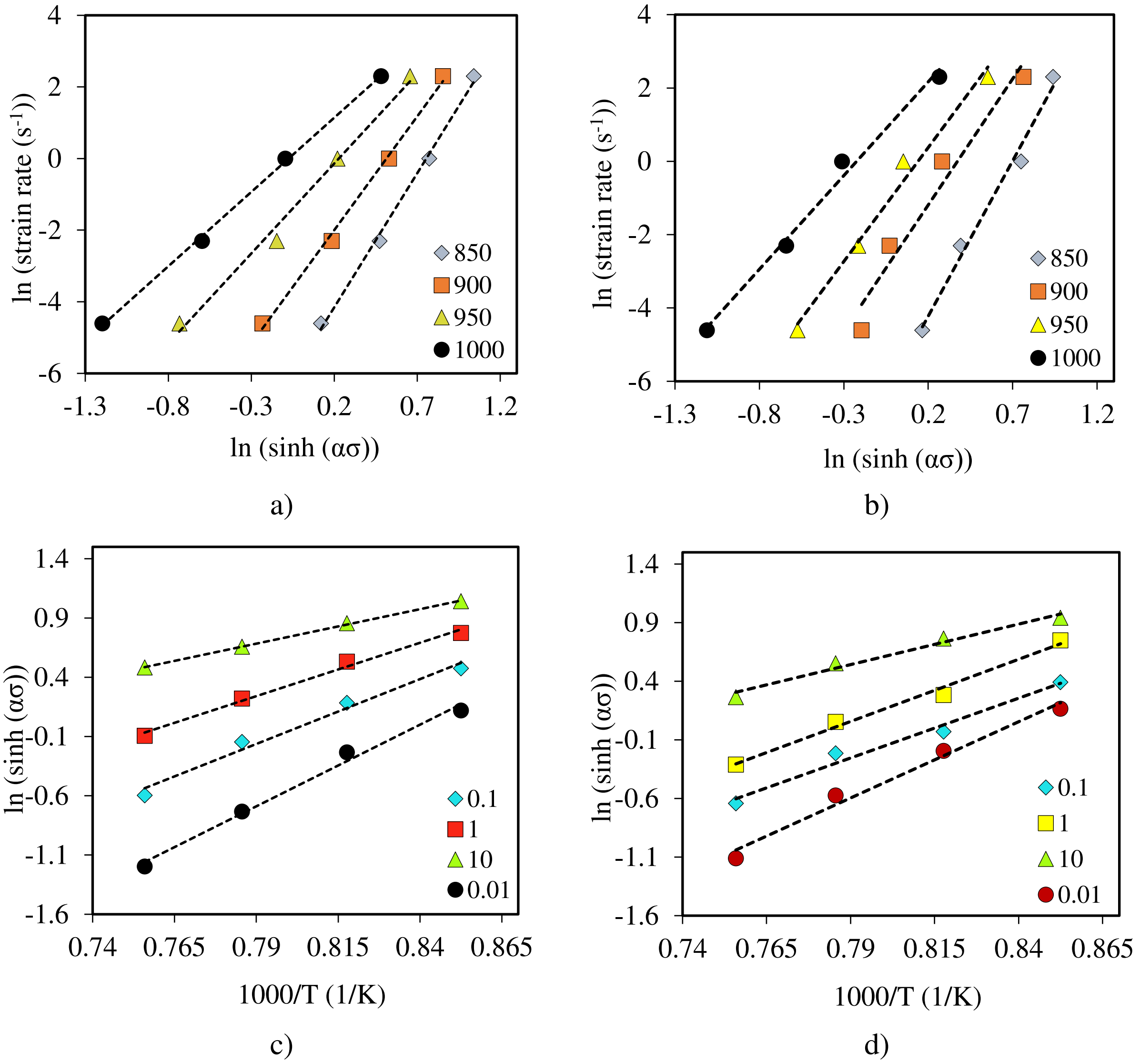

Figure 8. ((a) and (b)) plots of ln $\acute{\varepsilon}$ versus σ and ln (sinh (σα)) for determination of *n* and ((c) and (d)) are plots of ln (sinh (σα)) versus (1000)/T to determine *S* value for steel A and steel B respectively.

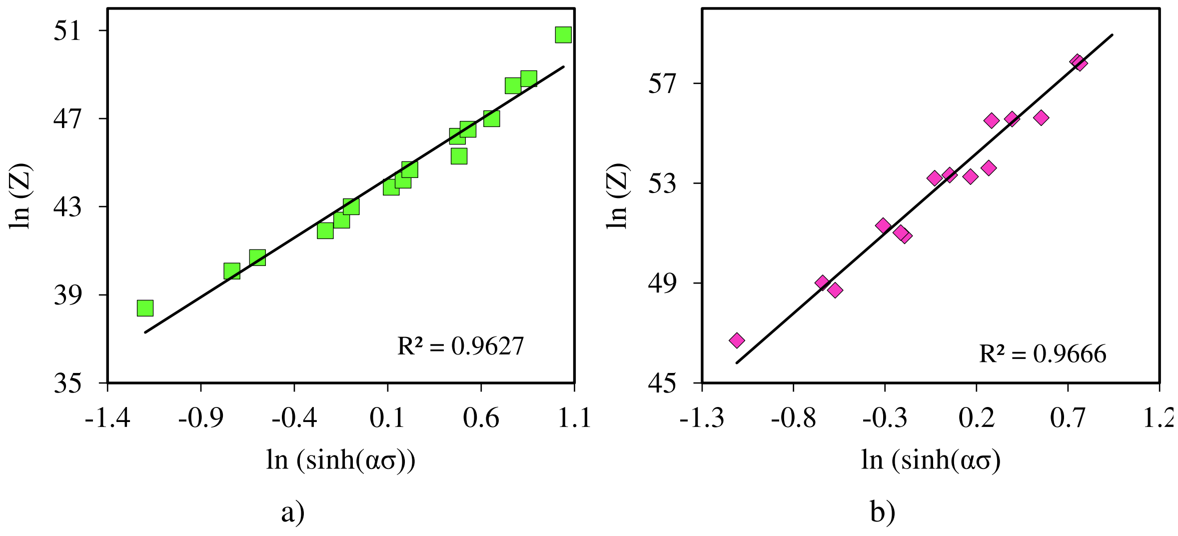

Figure 9. Plots of ln (Z) vs ln (sinh(ασ)) for a) Steel A and b) for steel B.

The calculated material constants for steel A and steel B for the constitutive equations are as given in **Error! Reference source not found.**.

Table 1. Material constants and activation energy for steel A and steel B.

P91	$\acute{\eta}$	β	η	α	S	$Q(kJmol^{-1})$	Ln A
Steel A	7.79	0.054	5.76	0.0069	9.89	473.08	9.98×10^{18}
Steel B	9.03	0.058	6.67	0.0065	10.18	564.48	9.58×10^{22}

3.3. Activation Energy and Stress Exponent

Error! Reference source not found. summarises the material constants n', β, n, S and activation energy, Q, for the two steels. The stress exponent and activation energy are termed apparent values. The term apparent implies that the constitutive equation does not consider the internal microstructure changes that occur during deformation, thus assuming constant metal flow behaviour. [44], [45]. The stress exponent, n and apparent activation energy, Q, indicate the deformation mechanisms that control the deformation process [46]. The activation energy shows the plastic workability of the material during the deformation process[47]. The difference between apparent and self-diffusion of Fe in austenite provides information on the dominant softening mechanisms during forging [47]. McQueen and Ryan [48] reported that the apparent activation energy is 20% higher than the self-diffusion activation energy when DRX is the dominant mechanism. The presence of precipitates, solutes, inclusions or reinforcements causes the activation energy to be 50% greater than the activation energy for self-diffusion. For high-stacking fault energy materials, the apparent activation energy is equivalent to or close to the activation energy for self-diffusion [38]. The results of this study show that the apparent activation energy for the two steels was: 473.08 kJ/mol (steel A) and 564.48 kJ/mol (steel B). In comparison, Q-value for the steel A was 65% greater than the self-diffusion activation energy of Fe in austenite (284 kJ/mol), while rejuvenated creep-exhaust steel was 98% higher. These results show that the two exhibited low plastic deformability.

The Q-values of the two steels show that the rejuvenated creep-exhausted steel has a higher resistance to deformation. The reason might be an incomplete dissolution of carbides during deformation. The presence of carbides impedes the deformation process by hindering dislocation movement and increases the stress exponent, n [49], [50]. The stress exponent obtained for steel B was 6.67 and for steel A was 5.76. The stress exponent is significantly affected by an increase in flow stress. Steel B that had higher flow stresses than steel A therefore had higher activation energy.

The stress exponent also shows the dynamic softening mechanisms involved during forming[46]. Zhou *et al*. [51] reported that when dislocation climb controls deformation, the stress exponent is 5, compared to 3 for dislocation glide mechanism controlled deformation. Dislocation climb and glide are dynamic softening mechanism showing that DRV occurred during deformation [52]. In this study, the flow stress-strain curves did not exhibit a clear flow stress peak. However, the flow curves exhibited a steady-state condition at higher strain as shown in **Error! Reference source not found.-Error! Reference source not found.**. Lower n-values (< 5) show that DRX was the dominant softening mechanism [42]. The stress exponent values shown in **Error! Reference source not found.** indicate that both WH+DRV controlled the deformation process. This deformation behaviour occurs in materials having high stacking fault energy, such as creep-resistant steel [53]. The difference between the steels may be due to the deformation conditions and steel chemistry. Higher n-values may be due to precipitates in the matrix, improving solid solution strengthening by pinning dislocation movement [2].

3.4. Constitutive Model of Flow Stresses

From materials constants and activation energy, Equations (15) and (16) are the constitutive models used to predict the flow stress behaviour of steel A and steel B, respectively.

$$\dot{\varepsilon} = 9.98 \times 10^{18}[Sinh\ (0.0069\sigma_{ss})]^{5.755175}\exp\left[\frac{-473.08}{RT}\right] \qquad (15)$$

$$\dot{\varepsilon} = 9.58 \times 10^{22}[Sinh\ (0.0065\sigma_{ss})]^{6.66945}\exp\left[\frac{-564.48}{RT}\right] \qquad (16)$$

Equation (17) shows the relationship between the flow stress and Zener-Hollomon parameter Z for steel A and steel B. The flow stress for the two steels can be obtained using Equations (18) for steel A and (19) for steel B.

$$\sigma = \frac{1}{\alpha} ln\left\{\left(\frac{Z}{A}\right)^{1/n} + \left[\left(\frac{Z}{A}\right)^{2/n} + 1\right]^{1/2}\right\} \qquad (17)$$

$$\sigma_{ss} = \frac{1}{0.0069} ln\left\{\left(\frac{Z}{9.98 \times 10^{18}}\right)^{1/5.76} + \left[\left(\frac{Z}{9.98 \times 10^{18}}\right)^{2/5.76} + 1\right]^{1/2}\right\} \qquad (18)$$

$$\sigma_{ss} = \frac{1}{0.0065} ln\left\{\left(\frac{Z}{9.58 \times 10^{22}}\right)^{1/6.66945} + \left[\left(\frac{Z}{9.58 \times 10^{22}}\right)^{2/6.67} + 1\right]^{1/2}\right\} \qquad (19)$$

3.5. Verification of Constitutive Models

The accuracy of constitutive equations (18) and (19) to predict flow stress was evaluated by comparing predicted to experimental data. **Error! Reference source not found.** a) and b) show graphical plots for the two equations obtained at different strain rates and temperatures. The graphs indicate a close correlation between the flow stresses (predicted and experimental) of these two steels investigated.

The accuracy of the developed equations to predict flow stress accurately was analysed using statistical parameters such as Pearson's correlation coefficient, *R* and Average Absolute Relative Error (AARE). Pearson's correlation coefficient, *R*, ranges between 0 and 1 and is determined using Equation (20) [54]. The proximity of R to 1 signifies a higher capability for the model to predict flow stress and vice versa. The *R*-value obtained for steel A was 0.97, and steel B was 0.98. *The R-value* obtained for both materials indicated a good correlation and a higher ability of the models to predict flow stress. These values compare well with the reports of other authors, such as Mwema *et al.*[55] and Samantaray *et al.* [22], with an *R*-value of 0.994.

Pearson's correlation coefficient, *R*, is liable to bias towards greater or lower values, hence resulting in misrepresenting the accuracy of the model to predict flow stresses[55]. Using the Average Absolute Relative Error (AARE) complements Pearson's correlation method and is less subject to bias[56]. AARE analyses errors for each predicted flow stress against experimental value on a case-by-case basis. Therefore, AARE is applied for each deformation condition to realise the statistical efficiency of the models developed. Therefore, AARE offers better reliability and presents unbiased statistical analysis[33]. Equation (21) provides means to calculate AARE as a percentage. A lower percentage value indicates a greater ability to predict flow stresses and vice versa. AARE obtained for the steel A was 7.62%, and for heat-treated creep-exhausted steel was 6.54%. Reports by other authors indicated marginally lower AARE findings for hot deformation of P91. Mwema *et al.*[55] obtained an AARE of 2.999%, and Samantaray *et al.* [22] had 5.27%. These variations are due to the differences in hot deformation parameters in the respective studies. The study by Mwema *et al.*[55] was for hot deformation temperature between 900 °C and 1200 °C and strain rate of 1s^{-1}, 5s^{-1}, 10s^{-1} and 15s^{-1}. In Samantaray *et al.* [22], the temperature for hot deformation was between 850 °C and 1100 °C and strain rates of 0.001s^{-1}, 0.1s^{-1} and 100s^{-1}. Validation by both models thus signified satisfactory levels of confidence in the respective constitutive equations to predict flow stresses.

$$R = \frac{\sum_{i=1}^{N}(P_i - P)(E_i - E)}{\sqrt{\sum_{i=1}^{N}(P_i - P)^2}\sqrt{\sum_{i=1}^{N}(E_i - E)^2}} \tag{20}$$

$$AARE = \frac{1}{N}\sum_{i=1}^{N}\left|\frac{E_i - P_i}{E_i}\right| \times 100\% \tag{21}$$

Where E_i is the flow stress from the experiment, P_i is the flow stress predicted from constitutive equations, E and P, are average flow stress values of experimental data E, and the predicted data P. N is the sum of data points.

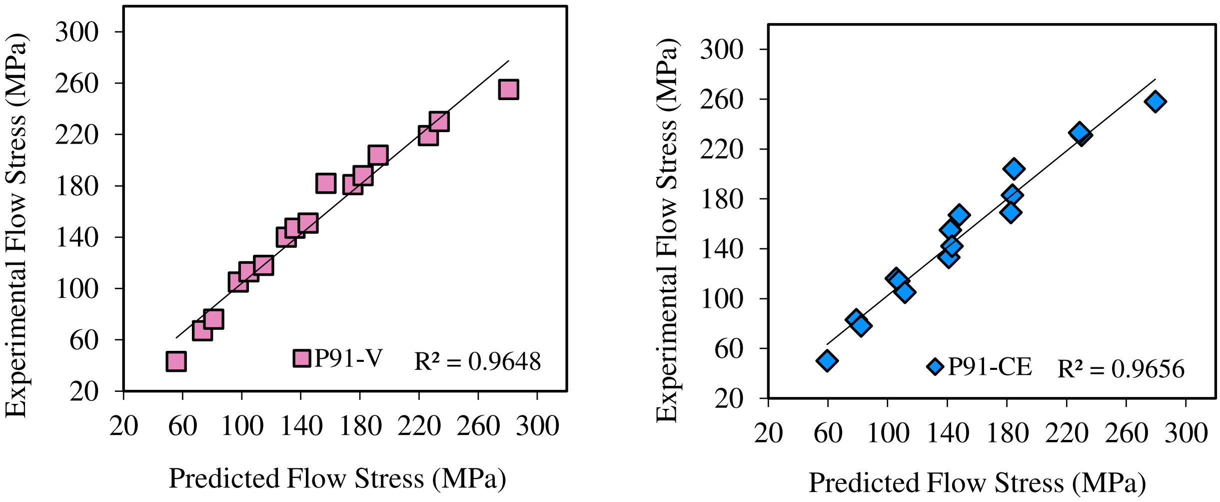

a) **b)**

Figure 10. Prediction of flow stress of mathematical models for a) Steel A and b) steel B.

3.6. Comparison of Constitutive Equations

The mathematical model developed for steel A was used to predict flow stresses of steel B and vice versa. The analysis intended to determine the suitability of having a model that can be applied to predict the flow stresses of either of the two steels investigated. **Error! Reference source not found.**a) is a plot of experimental stress versus the calculated flow stress where a model of steel A is used to predict the flow stress of steel B. From the statistical analysis, Pearson's correlation coefficient, *R*, was 0.9637, and AARE was 7.19%. Hence there was a good correlation between measured and predicted flow stress. The model for heat-treated creep-exhausted P91 steel was also used to predict flow stress for steel A (**Error! Reference source not found.** b)). The plot shows a good correlation between the measured and predicted flow stresses. Pearson's correlation coefficient was 0.95, and AARE was 8.36%. From the analysis, the steel A model had a better approximation than steel B model in predicting the flow stress for either P91 steel.

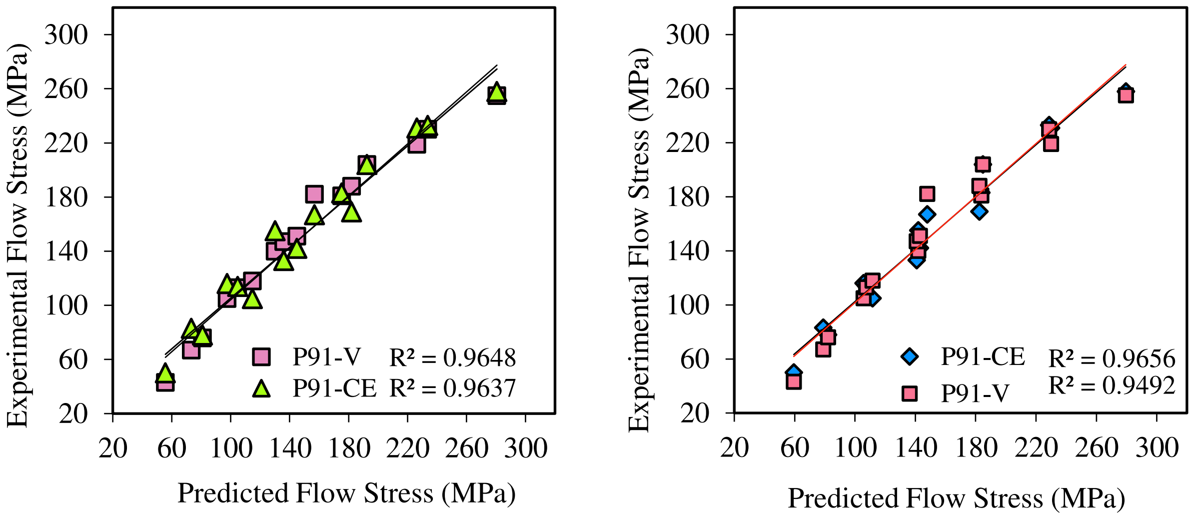

a) **b)**

Figure 11. a) Steel A model used to predict flow stresses of steel B b) Steel B model to predict flow stresses in Steel A.

4. Conclusion

In this study, the hot deformation behaviour of P91 steel was studied using a Gleeble® 3500 thermo-simulation machine on steel A and steel B. The deformation conditions were: a temperature range of 900°C to 1050°C and strain rates of 0.01 to 10s^{-1}. The findings are as itemised below:

1. The flow stress-strain curves show that the flow stress increased with an increase in strain rate (0.01 s^{-1} to 10s^{-1}) and decreased with an increase in temperature (900°C to 1050°C) for the two steels. The flow stress-strain curves exhibited a DRV+WH as the deformation mechanism.
2. The apparent activation energy of steel A was 473.08 kJ/mol, and for steel B was 564.48 kJ/mol. These Q-values were much higher compared to self-diffusion energy of iron in austenite (270 kJmol^{-1})
3. The mathematical constitutive models for steel A and steel B to strain of 0.6 are as given in Equation (22) and (23).

$$\dot{\varepsilon} = 9.97885 \times 10^{18}[Sinh\ (0.006916\sigma_{ss})]^{5.755175}\left[\frac{-473.0843}{RT}\right] \tag{22}$$

$$\dot{\varepsilon} = 9.58432 \times 10^{22}[Sinh\ (0.00647\sigma_{ss})]^{6.66945}\left[\frac{-564.4791}{RT}\right] \tag{23}$$

The constitutive models for steel A and steel B were used to predict flow stresses. The models were then validated using Pearson's correlation coefficient, R and Average Absolute Relative Error, AARE. For steel A, R was 0.97, and AARE was 7.62%. For heat-treated creep-exhausted P91 steel, R was 0.98, and AARE was 6.54%. These results show a good correlation between experimental and predicted values. The developed models for the two steels can be used interchangeably with acceptable accuracy. Using the model for steel A on steel B, Pearson's correlation coefficient was 0.96, and AARE was 7.19%. Similarly, using the steel B model on steel A, the R-value was 0.95, and AARE was 8.36%.

Data Availability Statement: The raw data presented in this study are available on request.

Acknowledgments: The authors would like to acknowledge and appreciate with gratitude the Dedan Kimathi University of Technology for financial contribution in facilitating this research.

Conflicts of Interest: The authors declare no conflict of interest.

References

1. N. Z. Gutiérrez, J. V. Alvarado, H. de Cicco, and A. Danón, “Microstructural Study of Welded Joints in a High Temperature Martensitic-ferritic ASTM A335 P91 Steel,” *Procedia Mater. Sci.*, 2015, vol. 8, no. 1992, pp. 1140–1149, doi: 10.1016/j.mspro.2015.04.178.
2. C. Pandey, M. Mohan, P. Kumar, and N. Saini, “Some studies on P91 steel and their weldments,” *J. Alloys Compd.*, 2018,vol. 743, pp. 332–364, doi: 10.1016/j.jallcom.2018.01.120.
3. A. Sharma, D. Kant Verma, and S. Kumaran, “Effect of post weld heat treatment on microstructure and mechanical properties of Hot Wire GTA welded joints of SA213 T91 steel,” *Mater. Today Proc.*, 2018, vol. 5, no. 2, pp. 8049–8056, doi: 10.1016/j.matpr.2017.11.490.
4. J. Oñoro, “Martensite microstructure of 9-12%Cr steels weld metals,” *J. Mater. Process. Technol.*, 2006, vol. 180, no. 1–3, pp. 137–142, doi: 10.1016/j.jmatprotec.2006.05.014.
5. G. Dak and C. Pandey, “A critical review on dissimilar welds joint between martensitic and austenitic steel for power plant application,” *J. Manuf. Process.*, 2020, vol. 58, no. August, pp. 377–406, doi: 10.1016/j.jmapro.2020.08.019.
6. C. Pandey, A. Giri, and M. M. Mahapatra, “Materials Science & Engineering A Evolution of phases in P91 steel in various heat treatment conditions and their effect on microstructure stability and mechanical properties,” *Mater. Sci. Eng. A*, 2016, vol. 664, pp. 58–74, doi: 10.1016/j.msea.2016.03.132.
7. A. Aghajani, C. Somsen, and G. Eggeler, “On the effect of long-term creep on the microstructure of a 12% chromium tempered martensite ferritic steel,” *Acta Mater.*, 2009, vol. 57, no. 17, pp. 5093–5106, doi: 10.1016/j.actamat.2009.07.010.
8. C. Pandey and M. M. Mahapatra, “Evolution of phases during tempering of P91 steel at 760°C for varying tempering time and their effect on microstructure and mechanical properties,” 2016,vol. 0, no. 0, pp. 1–21, doi: 10.1177/0954408916656678.
9. C. Hurtado-noreña, C. A. Danón, M. I. Luppo, and P. Bruzzoni, “Evolution of Minor Phases in a P91 Steel Normalized and Tempered at Different Temperatures,” *Procedia Mater. Sci.*, 2015, vol. 8, pp. 1089–1098, doi: 10.1016/j.mspro.2015.04.172.
10. L. Falat, L. Čiripová, V. Homolová, M. Džupon, R. Džunda, and K. Koval’, “The effects of various conditions of short-term rejuvenation heat treatment on room-temperature mechanical properties of thermally aged P92 boiler steel,” *Materials (Basel).*, 2021, vol. 14, no. 20, doi: 10.3390/ma14206076.
11. S. S. Hosseini, S. Nategh, and A. A. Ekrami, “Microstructural evolution in damaged IN738LC alloy during various steps of rejuvenation heat treatments,” *J. Alloys Compd.*, 2012, vol. 512, no. 1, pp. 340–350, doi: 10.1016/j.jallcom.2011.09.094.
12. A. Jamalpour, E. Hajjari, and S. M. Lari Baghal, “Effect of rejuvenation heat treatment on microstructure and hot corrosion resistance of a service-exposed nickel-based gas turbine blade,” *Mater. Res. Express*, 2019, vol. 6, no. 12, doi: 10.1088/2053-1591/ab6250.
13. R. Subbiah, M. Rahel, A. Sravika, R. Ambika, A. Srujana, and E. Navya, “Investigation on microstructure and mechanical properties of P91 alloy steel treated with normalizing process - A review,” *Mater. Today Proc.*, 2019, vol. 18, pp. 2265–2269, doi: 10.1016/j.matpr.2019.07.008.
14. N. G. Peng, B. Ahmad, M. R. Muhamad, and M. Ahadlin, “Phase Transformation Of P91 Steels Upon Cooling After Short Term Overheating Above Ac1 & Ac3 Temperature,” 2013, vol. 638, pp. 1756–1765, doi: 10.4028/www.scientific.net/AMR.634-638.1756.
15. G. Bakic *et al.*, “Material Characterization of the Main Steam Gate Valve Made of X20CrMoV 12.1 Steel after Long Term Service,” *Procedia Mater. Sci.*, 2020, vol. 3, no. September, pp. 1512–1517, 2014, doi: 10.1016/j.mspro.2014.06.244.
16. C. Pandey, A. Giri, and M. M. Mahapatra, “Materials Science & Engineering A Effect of normalizing temperature on microstructural stability and mechanical properties of creep strength enhanced ferritic P91 steel,” *Mater. Sci. Eng. A*, 2016, vol. 657, pp. 173–184, doi: 10.1016/j.msea.2016.01.066.
17. G. V. G. R. V Muthupandi, “Phase Transformation Behaviour in P91 During Post Weld Heat Treatment : A Gleeble Study,” *Trans. Indian Inst. Met.*, 2017, vol. 70, no. 3, pp. 875–885, doi: 10.1007/s12666-017-1075-0.
18. F. Abe, *Grade 91 heat-resistant martensitic steel*, 2014,vol. 91. Woodhead Publishing Limited.
19. C. Pandey, M. M. Mahapatra, P. Kumar, and N. Saini, “Materials Science & Engineering A Homogenization of P91 weldments using varying normalizing and tempering treatment,” *Mater. Sci. Eng. A*, 2017, vol. 710, no. June pp. 86–101, 2018, doi: 10.1016/j.msea.2017.10.086.
20. J. Hald, “Microstructure and long-term creep properties of 9-12% Cr steels,” *Int. J. Press. Vessel. Pip.*, 2008, vol. 85, no. 1–2, pp. 30–37, doi: 10.1016/j.ijpvp.2007.06.010.
21. W. Yan, W. Wang, Y. Y. Shan, and K. Yang, “Microstructural stability of 9-12%Cr ferrite/martensite heat-resistant steels,” *Front. Mater. Sci.*, vol. 7, no. 1, pp. 1–27, 2013, doi: 10.1007/s11706-013-0189-5.
22. D. Samantaray, S. Mandal, and A. K. Bhaduri, “Constitutive analysis to predict high-temperature flow

stress in modified 9Cr-1Mo (P91) steel," *Mater. Des.*, 2010, vol. 31, no. 2, pp. 981–984, doi: 10.1016/j.matdes.2009.08.012.

23. X. Niu, L. Shen, C. Chen, J. Zhou, and L. Chen, "An Arrhenius - type constitutive model to predict the deformation behavior of Sn0 . 3Ag0 . 7Cu under different temperature," *J. Mater. Sci. Mater. Electron.*, 2019, vol. 2, no. 0123456789, doi: 10.1007/s10854-019-01833-9.
24. G. Z. Quan, G. S. Li, Y. Wang, W. Q. Lv, C. T. Yu, and J. Zhou, "A characterization for the flow behavior of as-extruded 7075 Aluminum alloy by the improved arrhenius model with variable parameters," *Mater. Res.*, 2013, vol. 16, no. 1, pp. 19–27, doi: 10.1590/S1516-14392012005000156.
25. X. Yang and W. Li, "Flow Behavior and Processing Maps of a Low-Carbon Steel During Hot Deformation," *Metall. Mater. Trans. A Phys. Metall. Mater. Sci.*, 2015, vol. 46, no. 12, pp. 6052–6064, doi: 10.1007/s11661-015-3190-z.
26. L. Xu, D. Zhang, Y. Liu, B. Ning, Z. Qiao, Z. Yan and H. Li., "Precipitation kinetics of $M_{23}C_6$ in T/P92 heat-resistant steel by applying soft-impingement correction," *J. Mater. Res.*, 2013, vol. 28, no. 11, pp. 1529–1537, doi: 10.1557/jmr.2013.116.
27. A. Anitha Lakshmi, C. Srinivasa Rao, J. Gangadhar, C. Srinivasu, and S. K. Singh, "Review of Processing Maps and Development of Qualitative Processing Maps," *Mater. Today Proc.*, 2017, vol. 4, no. 2, pp. 946–956, doi: 10.1016/j.matpr.2017.01.106.
28. Y. V. R. K. Prasad and K. P. Rao, "Processing maps for hot deformation of rolled AZ31 magnesium alloy plate: Anisotropy of hot workability," *Mater. Sci. Eng. A*, 2008, vol. 487, no. 1–2, pp. 316–327, doi: 10.1016/j.msea.2007.10.038.
29. Z. B. Xiao, Y. C. Huang, and Y. Liu, "Modeling of Flow Stress of 2026 Al Alloy under Hot Compression," *Adv. Mater. Sci. Eng.*, 2016, vol. 2016, pp. 28–32, doi: 10.1155/2016/3803472.
30. J. Obiko, "Friction correction of flow stress-strain curve in the upsetting process," *IOP SciNotes*, 2021, vol. 2, no. 1, p. 014401, doi: 10.1088/2633-1357/abdd96.
31. Y. Li, E. Onodera, and A. Chiba, "Friction coefficient in hot compression of cylindrical sample," *Mater. Trans.*, 2010, vol. 51, no. 7, pp. 1210–1215, doi: 10.2320/matertrans.M2010056.
32. B. Roebuck, J. D. Lord, M. Brooks, M. S. Loveday, C. M. Sellars, and R. W. Evans, "Measurement of flow stress in hot axisymmetric compression tests," *Mater. High Temp.*, 2006, vol. 23, no. 2, pp. 59–83, doi: 10.1179/mht.2006.005.
33. S. Ghosh, M. Chandra, S. Daria, and S. Suhrit, "Hot Deformation Characteristic and Strain Dependent Constitutive Flow Stress Modelling of Ti + Nb Stabilized Interstitial Free Steel," *Met. Mater. Int.*, 2020, no. 0123456789, doi: 10.1007/s12540-020-00827-1.
34. M. Hu, "Correction of Flow Curves and Constitutive Modelling of a Ti-6Al-4V Alloy," pp. 1–15, 2018, doi: 10.3390/met8040256.
35. D. Samantaray, S. Mandal, and A. K. Bhaduri, "Optimization of hot working parameters for thermo-mechanical processing of modified 9Cr-1Mo (P91) steel employing dynamic materials model," *Mater. Sci. Eng. A*, 2011,vol. 528, no. 15, pp. 5204–5211, doi: 10.1016/j.msea.2011.03.025.
36. J. J. Jonas, X. Quelennec, L. Jiang, and É. Martin, "The Avrami kinetics of dynamic recrystallization," *Acta Mater.*, 2009,vol. 57, no. 9, pp. 2748–2756, doi: 10.1016/j.actamat.2009.02.033.
37. Z. Li, H. Xie, F. Jia, Y. Lu, X. Yuan, S. Jiao and Z. Jiang, "Study on deformation characteristics and microstructure evolution of 2205/AH36 bimetal composite in a novel hot forming process," *Metals (Basel).*, 2020, vol. 10, no. 10, pp. 1–17, doi: 10.3390/met10101375.
38. M. O. Bodunrin, L. H. Chown, J. W. van der Merwe, and K. K. Alaneme, "Hot working behaviour of experimental Ti-4.5Al-1 V-3Fe alloy with initial lamellar microstructure," *Int. J. Adv. Manuf. Technol.*, 2020, vol. 106, no. 5–6, pp. 1901–1916, doi: 10.1007/s00170-019-04718-7.
39. J. Obiko, L. Chown, D. Whitefield, and M. Bodunrin, "Understanding hot workability of power plant P92 creep resistant steels using dynamic material modelling (DMM) and microstructural evolution," *Int. J. Interact. Des. Manuf.*, 2022, doi: 10.1007/s12008-022-01084-9.
40. J. Obiko, L. H. Chown, and D. J. Whitefield, "Warm deformation behaviour of P92 steel," *Mater. Res. Express*, 2019, vol. 6, no. 12, doi: 10.1088/2053-1591/ab5e9c.
41. M. O. Bodunrin, "Flow stress prediction using hyperbolic-sine Arrhenius constants optimised by simple generalised reduced gradient refinement," *J. Mater. Res. Technol.*, 2020, vol. 9, no. 2, pp. 2376–2386, doi: 10.1016/j.jmrt.2019.12.070.
42. H. Mirzadeh, J. M. Cabrera, and A. Najafizadeh, "Constitutive relationships for hot deformation of austenite," *Acta Mater.*, 2011, vol. 59, no. 16, pp. 6441–6448, doi: 10.1016/j.actamat.2011.07.008.
43. C. M. Sellars and W. J. McTegart, "On the mechanism of hot deformation," *Acta Metall.*, 1966, vol. 14, no. 9, pp. 1136–1138, doi: 10.1016/0001-6160(66)90207-0.
44. J. M. Cabrera, J. J. Jonas, and J. M. Prado, "Flow behaviour of medium carbon microalloyed steel under hot

working conditions," *Mater. Sci. Technol.*, 1996, vol. 12, no. 7, pp. 579–585, doi: 10.1179/mst.1996.12.7.579.

45. R. Baktash and H. Mirzadeh, "A Simple Constitutive Model for Prediction of Single-Peak Flow Curves Under Hot Working Conditions," *J. Eng. Mater. Technol. Trans. ASME*, 2016, vol. 138, no. 2, doi: 10.1115/1.4032153.
46. Z. Akbari, H. Mirzadeh, and J. M. Cabrera, "A simple constitutive model for predicting flow stress of medium carbon microalloyed steel during hot deformation," *Mater. Des.*, 2015, vol. 77, pp. 126–131, doi: 10.1016/j.matdes.2015.04.005.
47. K. K. Alaneme, S. A. Babalola, and M. O. Bodunrin, "On the prediction of hot deformation mechanisms and workability in Al6063/Nip and Al6063/steelp composites using hyperbolic-sine constitutive equation," *Mater. Today Proc.*, 2021, vol. 38, no. xxxx, pp. 942–948, doi: 10.1016/j.matpr.2020.05.463.
48. H. J. McQueen and N. D. Ryan, "Constitutive analysis in hot working," *Mater. Sci. Eng. A*, 2002, vol. 322, no. 1–2, pp. 43–63, doi: 10.1016/S0921-5093(01)01117-0.
49. C. Menapace, N. Sartori, M. Pellizzari, and G. Straffelini, "Hot Deformation Behavior of Four Steels: A Comparative Study," *J. Eng. Mater. Technol. Trans. ASME*, 2018, vol. 140, no. 2, doi: 10.1115/1.4038670.
50. M. Carsí, F. Peñalba, I. Rieiro, and O. A. Ruano, "High temperature workability behavior of a modified P92 steel," *Int. J. Mater. Res.*, 2011, vol. 102, no. 11, pp. 1378–1383, doi: 10.3139/146.110603.
51. D. Q. Zhou, X. Q. Xu, H. H. Mao, Y. F. Yan, T. G. Nieh, and Z. P. Lu, "Materials Science & Engineering A Plastic fl ow behaviour in an alumina-forming austenitic stainless steel at elevated temperatures," 2014, vol. 594, pp. 246–252, doi: 10.1016/j.msea.2013.11.021.
52. S. V. Mehtonen, L. P. Karjalainen, and D. A. Porter, "Hot deformation behavior and microstructure evolution of a stabilized high-Cr ferritic stainless steel," *Mater. Sci. Eng. A*, 2013, vol. 571, pp. 1–12, doi: 10.1016/j.msea.2013.01.077.
53. J. O. Obiko, F. M. Mwema, and H. Shangwira, "Forging optimisation process using numerical simulation and Taguchi method," *SN Appl. Sci.*, 2020, vol. 2, no. 4, doi: 10.1007/s42452-020-2547-0.
54. F. Gao, Z. Liu, R. D. K. Misra, H. Liu, and F. Yu, "Constitutive modeling and dynamic softening mechanism during hot deformation of an ultra-pure 17%Cr ferritic stainless steel stabilized with Nb," *Met. Mater. Int.*, 2014, vol. 20, no. 5, pp. 939–951, doi: 10.1007/s12540-014-5020-z.
55. F. M. Mwema *et al.*, "Constitutive analysis of hot forming process of P91 steel: finite element method approach," *Adv. Mater. Process. Technol.*, 2021, vol. 00, no. 00, pp. 1–12, doi: 10.1080/2374068X.2021.1939560.
56. J. Cai, F. Li, T. Liu, B. Chen, and M. He, "Constitutive equations for elevated temperature flow stress of Ti-6Al-4V alloy considering the effect of strain," *Mater. Des.*, 2011, vol. 32, no. 3, pp. 1144–1151, doi: 10.1016/j.matdes.2010.11.004.